

Article

Hollow $\text{CuFe}_2\text{O}_4/\text{MgFe}_2\text{O}_4$ Heterojunction Boost Photocatalytic Oxidation Activity for Organic Pollutants

Zhicheng Zhang¹, Wei Cai¹, Shaopeng Rong², Hongxia Qu^{1,*} and Huifang Xie^{2,*}

¹ Department of Chemical Engineering and Technology, School of Chemistry and Chemical Engineering, Nanjing University of Science and Technology, Nanjing 210094, China

² Department of Environmental Science and Technology, School of Environmental and Biological Engineering, Nanjing University of Science and Technology, Nanjing 210094, China

* Correspondence: qhx@mail.njust.edu.cn (H.Q.); huifangxie@hotmail.com (H.X.)

Abstract: P-n heterojunction-structured $\text{CuFe}_2\text{O}_4/\text{MgFe}_2\text{O}_4$ hollow spheres with a diameter of 250 nm were synthesized using a template-free solvothermal method, and time-dependent morphological studies were carried out to investigate the hollow formation mechanism. The $\text{CuFe}_2\text{O}_4/\text{MgFe}_2\text{O}_4$ with a molar ratio of 1:2 (Cu:Mg) had the highest degradation efficiency with the model organic dye Acid Orange 7, with a degradation rate of 91.96% over 60 min. The synthesized $\text{CuFe}_2\text{O}_4/\text{MgFe}_2\text{O}_4$ nanocomposites were characterized by XRD, TEM, HRTEM, UV-vis spectroscopy, Mott-Schottky, and EIS. Due to the synthesis of the p-n heterojunction, $\text{CuFe}_2\text{O}_4/\text{MgFe}_2\text{O}_4$ has efficient photogenerated carriers, and the hollow structure has a higher specific surface area and stronger adsorption capacity, which is significantly better than that of CuFe_2O_4 and MgFe_2O_4 in terms of photocatalytic performance. The outstanding performance shows that the p-n heterostructure of $\text{CuFe}_2\text{O}_4/\text{MgFe}_2\text{O}_4$ has potential for application in wastewater degradation.

Keywords: copper ferrite; magnesium ferrite; p-n junction; photocatalytic oxidation; hollow microspheres



Citation: Zhang, Z.; Cai, W.; Rong, S.; Qu, H.; Xie, H. Hollow $\text{CuFe}_2\text{O}_4/\text{MgFe}_2\text{O}_4$ Heterojunction Boost Photocatalytic Oxidation Activity for Organic Pollutants. *Catalysts* **2022**, *12*, 910. <https://doi.org/10.3390/catal12080910>

Academic Editor: Rufino M. Navarro Yerga

Received: 29 July 2022

Accepted: 17 August 2022

Published: 18 August 2022

Publisher's Note: MDPI stays neutral with regard to jurisdictional claims in published maps and institutional affiliations.



Copyright: © 2022 by the authors. Licensee MDPI, Basel, Switzerland. This article is an open access article distributed under the terms and conditions of the Creative Commons Attribution (CC BY) license (<https://creativecommons.org/licenses/by/4.0/>).

1. Introduction

In today's world, many chemical organic pollutants (dyes) are released into water bodies every year, which are difficult to degrade completely [1–5]. Advanced photocatalytic oxidation technology with a strong oxidizing ability and high efficiency is considered as a very promising means of wastewater treatment for the degradation of organic pollutants [6–8]. Light-induced photocatalytic activity and magnetic separation have potential as low-cost [9], high-efficiency [10–13], and high-stability [14,15] methods of water remediation. The hollow microsphere structure is one of the areas of focus in the field of catalysis at present, because the hollow microsphere structure has better structural properties than the solid sphere structure, according to the following considerations: (1) compared with solid microspheres, the hollow microsphere structure has a larger specific surface area and stronger adsorption capacity [16]; (2) the cavity structure can confine the catalytic reaction to the reactants, improving the stability of the reaction and the efficiency of the catalytic reaction [17,18]; (3) the photon can remain in the shell structure for a longer time, with a higher utilization rate [17,18]; and (4) the shell structure can also be beneficial for the diffusion of reactant molecules in the hollow microspheres and increase the contact area between the reactant and the catalyst [16,18].

In order to further improve their photocatalytic degradation efficiency, researchers have further promoted the separation of photogenerated carriers by designing a heterojunction structure, which improves the conversion efficiency of the solar energy [19,20]. Heterojunction photocatalysts are formed by coupling two semiconductor photocatalysts with complementary properties, relative band positions, and differences in fermi levels [21]. This method facilitates the separation of the electron-hole pairs [19,22,23], expands the absorbable spectral range [19], and enhances the redox capacity [20], thereby compensating

for the shortcomings of a single semiconductor [23]. Yin et al. [15] prepared an all-solid-state hybrid photocatalyst, Au@CdS/U-WO₃, with a unique sea urchin-like micro-nano heterostructure, without adding additives by the continuous photo deposition of Au and CdS on the WO₃ supports, which significantly improved the photocatalytic hydrogen evolution activity. Zhu et al. [13] successfully synthesized a series of MA₃Bi₂Br₉-COFs nanocomposites with a variety of B sites and different ratios of PNCs via a facile in situ growth approach. The MA₃Bi₂Br₉-COFs nanocomposites efficiently photocatalyzed the polymerization of various functional monomers with the assistance of a large scope of co-initiators via both electron and hole transfer mechanisms in both aqueous and organic media, achieving a considerable conversion rate of up to 97.5%. Ferrites are one of the most efficient solid metal oxide photocatalysts and are commonly used to synthesize heterojunction-structured catalysts [24–27]. The homogeneous and heterogeneous ferrite composites CaFe₂O₄/MgFe₂O₄ [28] and ZnFe₂O₄/MoS₂ [29] have been reported to exhibit enhanced visible-light photocatalysis. Spinel ferrite CuFe₂O₄ is a structurally stable heterogeneous catalytic material, which has many advantages, such as good magnetic properties, a small band gap, high chemical stability, low price, safety and environmentally protective properties [30,31]. The cycle activity of Cu²⁺/Cu⁺ is higher than that of Fe³⁺/Fe²⁺, and it can catalyze the production of ·OH from H₂O₂. Shen et al. [32] successfully prepared CuFe₂O₄ microspheres with a particle size of 116 nm using a solvothermal method, which exhibited good photocatalytic properties. Sharma et al. [33] experimentally verified that CuFe₂O₄ has the best photocatalytic performance compared to the spinel ferrite MFe₂O₄ (M = Cu, Zn, Ni, Co) nanoparticles. MgFe₂O₄ nanoparticles have attracted extensive attention due to their chemical properties, reproducibility, and magnetic properties. Due to these unique properties, they have a wide range of applications, including magnetic technology and heterogeneous catalysts [26,34]. CuFe₂O₄ and MgFe₂O₄ have similar crystalline features. However, they have different band structures. CuFe₂O₄ is a p-type semiconductor with a narrow band gap (E_g) of 1.32~1.69 eV [32,35,36], while MgFe₂O₄ is an n-type semiconductor with a wide band gap (E_g) of 1.9~2.56 eV [28,29,37]. Forming a p-n heterojunction is an ideal method for preventing the recombination of charges, and consequently enhancing the photocatalytic ability of materials [38–41]. Here, CuFe₂O₄ and MgFe₂O₄ were chosen for the fabrication of photocatalysts with p-n heterojunctions to enhance their photocatalytic activity.

Herein, the polyethylene glycol-20000 (PEG-20000)-assisted hydrothermal method was successfully developed to prepare hollow spheres of the homo ferrite composite of CuFe₂O₄/MgFe₂O₄. The physicochemical properties of the products were characterized, and the photocatalytic activities were evaluated by degrading the model organic dye Acid Orange 7 (AO₇) under visible-light irradiation. In addition, the active species in the photocatalytic process were discussed, and the possible mechanism was proposed.

2. Results and Discussion

2.1. Fabrication of Hollow CuFe₂O₄/MgFe₂O₄ and Its Structure

The TEM images of CuFe₂O₄/MgFe₂O₄ with different Cu/Mg ratios in the precursors are shown in Figure 1. It can be seen that all samples formed hollow spherical structures with rough surfaces and wormholes between the fine grains. This kind of structure can contribute to the higher surface area [42], more active sites, easier mass diffusion and transport, lighter penetration and higher quantum efficiency of the photocatalytic reaction in the application process [16]. The diameter of the microspheres was 200–300 nm and the agglomeration of the hollow spherical structures can be attributed to the magnetic characteristics of the particles [43]. The cavity size gradually increased with an increasing Mg ratio, and when the ratio of CuFe₂O₄/MgFe₂O₄ reached 1:2, the cavity size no longer varied and reached about 100 nm. It can be seen from Table S1 that the Cu/Mg molar ratio in CuFe₂O₄/MgFe₂O₄ was close to the feeding ratio. Although the catalyst particle size was different, as seen from the TEM images, it had little effect on the photo reaction performance and reproducibility, as shown in Figure S2.

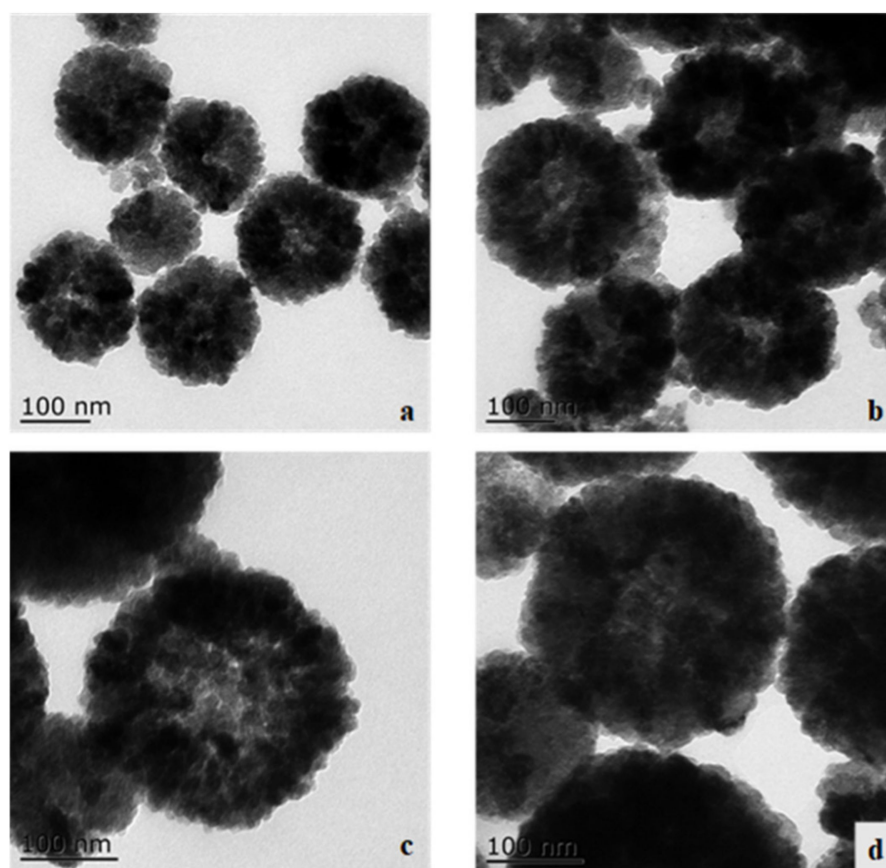


Figure 1. TEM images of $\text{CuFe}_2\text{O}_4/\text{MgFe}_2\text{O}_4$: (a) Cu:Mg = 1:0.5; (b) Cu:Mg = 1:1; (c) Cu:Mg = 1:2; (d) Cu:Mg = 1:3.

The structures of the hollow $\text{CuFe}_2\text{O}_4/\text{MgFe}_2\text{O}_4$ at different preparation times are shown in Figure 2a–c. A comparison of the different plots shows that the microstructure of the $\text{CuFe}_2\text{O}_4/\text{MgFe}_2\text{O}_4$ composite gradually expanded from a smaller solid spherical structure to a hollow spherical structure with a larger diameter, and the spherical surface gradually became smooth with an increasing preparation time under the same preparation conditions. However, when the reaction time reached 12 h, the smaller particles covered the surface of the larger particles, resulting in the observed hollow structure becoming blurred. Here, the introduction of PEG-20000 provided nucleation sites for the ferrite growth, and the hollowing process was similar to Ostwald ripening [16]. Therefore, 8 h of PEG-assisted hydrothermal synthesis was chosen as the time for the preparation of the hollow and homogeneous ferrite composites. The high-resolution TEM (HRTEM) image of $\text{CuFe}_2\text{O}_4/\text{MgFe}_2\text{O}_4$ (Figure 2d) clearly shows that CuFe_2O_4 had successfully formed a heterojunction structure with MgFe_2O_4 . Clear lattice fringes with lattice spacings of 0.25 and 0.17 nm can be observed in the (311) crystal plane of CuFe_2O_4 and the (422) crystallographic plane of MgFe_2O_4 , respectively [32,44,45]. It has also been observed that a close relationship exists between CuFe_2O_4 and MgFe_2O_4 , which is expected to favor the formation of heterojunctions between CuFe_2O_4 and MgFe_2O_4 , leading to a better interfacial charge transfer [46]. From this, it can be inferred that p-n junctions are formed when p-type CuFe_2O_4 and n-type MgFe_2O_4 are in close contact. At the same time, an internal electric field is established on their contact surfaces [47].

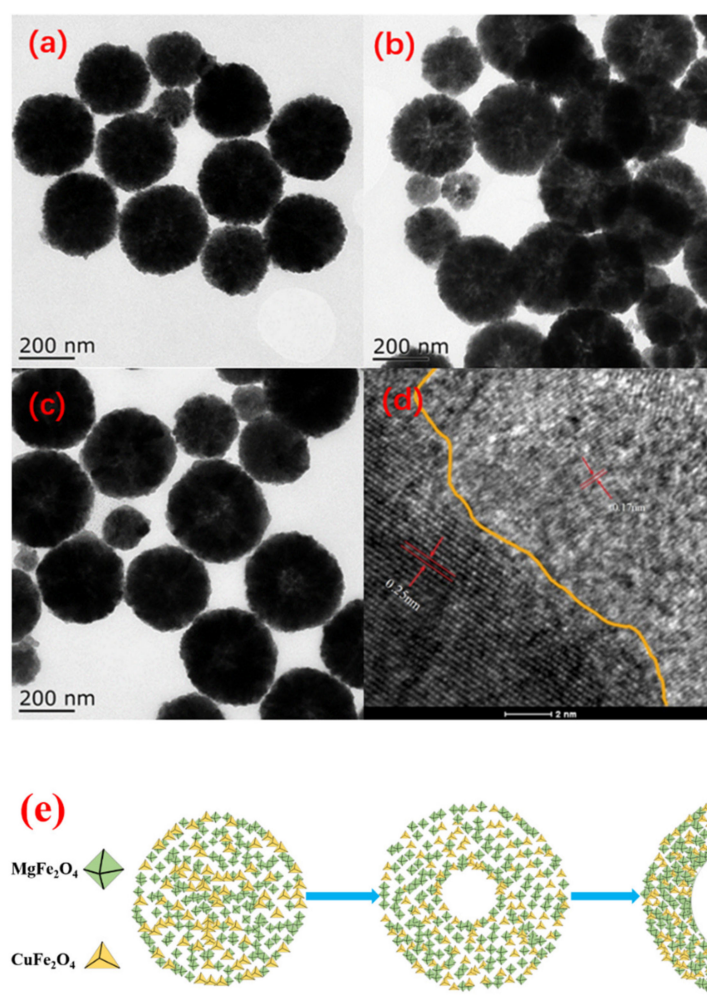


Figure 2. TEM images of (1:2) $\text{CuFe}_2\text{O}_4/\text{MgFe}_2\text{O}_4$: (a) 4 h with PEG; (b) 8 h with PEG; (c) 12 h with PEG; (d) HRTEM image; (e) schematic illustration (downward views) of the ripening process of the hollow structures.

Based on the appearance of the hollow microspheres observed in the TEM images at different times, a possible mechanism for the formation of $\text{CuFe}_2\text{O}_4/\text{MgFe}_2\text{O}_4$ hollow nanospheres can be proposed, as shown in Figure 2e. In the present experiments, PEG-20000 played a role in inducing the crystallization of metallic elements. In the early stage of the reaction, as shown in Figure 2a, many smaller microcrystals were tightly packed in the $\text{CuFe}_2\text{O}_4/\text{MgFe}_2\text{O}_4$ spheres, forming a solid microsphere structure of solid spheres with a high external surface energy but minimal internal surface energy. As the reaction time increased, the inner central region of the solid spheres started to dissolve and evacuate to the outer surface, and the Ostwald ripening process occurred. The gradual dissolution of the internal small crystals and the continuous external diffusion resulting in recrystallization led to the formation of hollow cavities and the emergence of $\text{CuFe}_2\text{O}_4/\text{MgFe}_2\text{O}_4$ hollow nanosphere structures. When the reaction time continued to increase, as shown in Figure 2b, the surface energy of the outer surface of the hollow nanospheres gradually stabilized and the cavity structure no longer became larger. At this time, the cavity diameter reached about 100 nm; thus, 8 h should be identified as the optimal solvent heat time.

The XRD patterns of the complexes with different molar ratios of CuFe_2O_4 and MgFe_2O_4 are shown in Figure 3. All samples had obvious characteristic peaks at 2θ of 30.1° , 35.6° , 43.4° , 56.9° and 63.6° , ascribed to the (220), (311), (400), (551) and (440) lattice planes of CuFe_2O_4 (JCPDS No. 25-0283) and MgFe_2O_4 (JCPDS No. 88-1936). CuFe_2O_4 (Figure S1a) had a cube phase (Lattice parameters; $\alpha = 119.559^\circ$, $\beta = 119.557^\circ$, $\gamma = 90.763^\circ$)

and MgFe_2O_4 (Figure S1b) had an orthorhombic phase (Lattice parameters; $\alpha = 120.114^\circ$, $\beta = 119.940^\circ$, $\gamma = 89.953^\circ$) [28]. Due to the fact that the cell volume of MgFe_2O_4 (154.342 \AA^3) is larger than that of CuFe_2O_4 (153.730 \AA^3), with the addition of the Mg content, the characteristic diffraction peaks of the composite shifted to lower angles, which means that the crystal spacing of the composites increased. Similar results have also been reported in regard to the $\text{CaFe}_2\text{O}_4/\text{MgFe}_2\text{O}_4$ heterojunction [28].

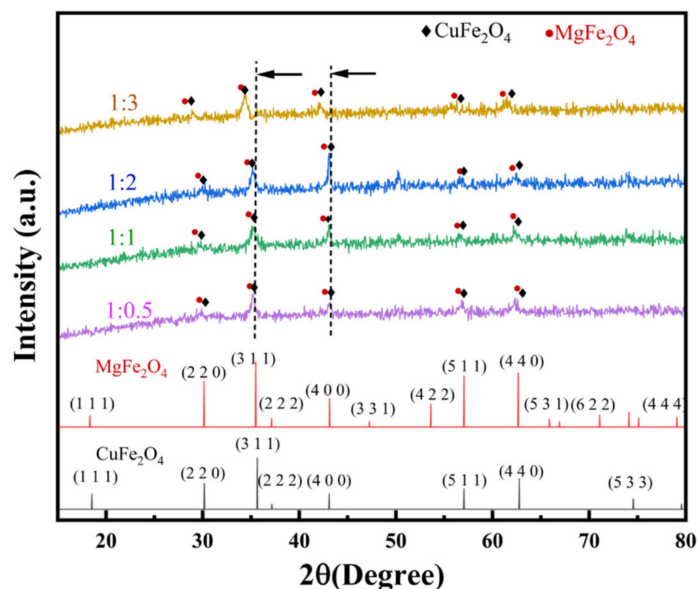


Figure 3. XRD patterns of all $\text{CuFe}_2\text{O}_4/\text{MgFe}_2\text{O}_4$ samples.

2.2. Optical Properties of the Hollow $\text{CuFe}_2\text{O}_4/\text{MgFe}_2\text{O}_4$

The effect of the heterogeneous binding of n- MgFe_2O_4 and p- CuFe_2O_4 on the visible light capture ability was investigated by UV-vis diffuse reflectance spectroscopy, as shown in Figure 4a. The absorption edges of MgFe_2O_4 and CuFe_2O_4 in the visible light absorption region were 471 nm and 486 nm, respectively. Moreover, the absorption edge of $\text{CuFe}_2\text{O}_4/\text{MgFe}_2\text{O}_4$ had a significant red shift increase compared to MgFe_2O_4 , which indicates that the p-n $\text{CuFe}_2\text{O}_4/\text{MgFe}_2\text{O}_4$ photocatalyst had a higher visible light absorption ability. The band gaps of $\text{CuFe}_2\text{O}_4/\text{MgFe}_2\text{O}_4$ were obtained from Equation (8).

As shown in Figure 4b,c, the band gaps of n- MgFe_2O_4 and p- CuFe_2O_4 were 1.48 eV and 2.06 eV, respectively. However, for the $\text{CuFe}_2\text{O}_4/\text{MgFe}_2\text{O}_4$ composite, as illustrated in Figure 4d, the band positions of both CuFe_2O_4 and MgFe_2O_4 were shifted to ensure Fermi levels reached the new balanced state, respectively, which resulted in the final electronic structure of the p-n heterojunction [48].

As shown in Figure 5a, the impedance of the $\text{CuFe}_2\text{O}_4/\text{MgFe}_2\text{O}_4$ heterojunction structure was significantly lower than that of MgFe_2O_4 and CuFe_2O_4 , indicating that the synthesis of the p-n junctions accelerated the process of interfacial charge transfer. This result indicates that the p-n junction structure promoted the separation and electron transfer of photogenerated carriers. To determine the position of the energy band edges of the obtained samples and to verify the p-n heterojunctions, Mott–Schottky measurements were performed on CuFe_2O_4 , MgFe_2O_4 , and $\text{CuFe}_2\text{O}_4/\text{MgFe}_2\text{O}_4$ samples. As shown in Figure 5b–d, the Mott–Schottky plot of CuFe_2O_4 has a negative slope, corresponding to a typical p-type with a flat-band voltage of 0.72 eV (vs. SCE). The Mott–Schottky plot of MgFe_2O_4 has a positive slope and corresponds to a typical n-type with a flat-band voltage of -0.49 eV (vs. SCE). As a characteristic of p-type semiconductors, the flat band potential of CuFe_2O_4 can be attributed to the valence band maximum (VBM), while the associated value of MgFe_2O_4 can be attributed to the conduction band minimum (CBM) [48].

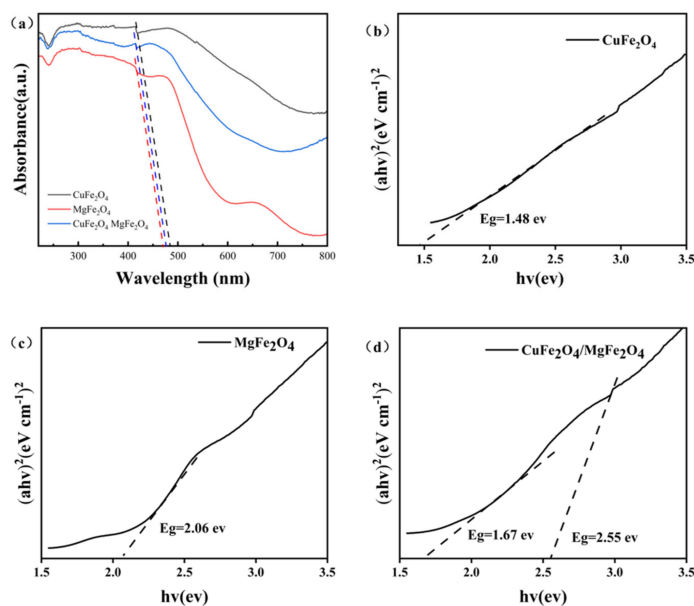


Figure 4. (a) UV-vis DRS of the pure CuFe₂O₄, MgFe₂O₄ and CuFe₂O₄/MgFe₂O₄ composites; (b–d) plots of (αhν)² versus photon energy (hν) for CuFe₂O₄, MgFe₂O₄ and CuFe₂O₄/MgFe₂O₄.

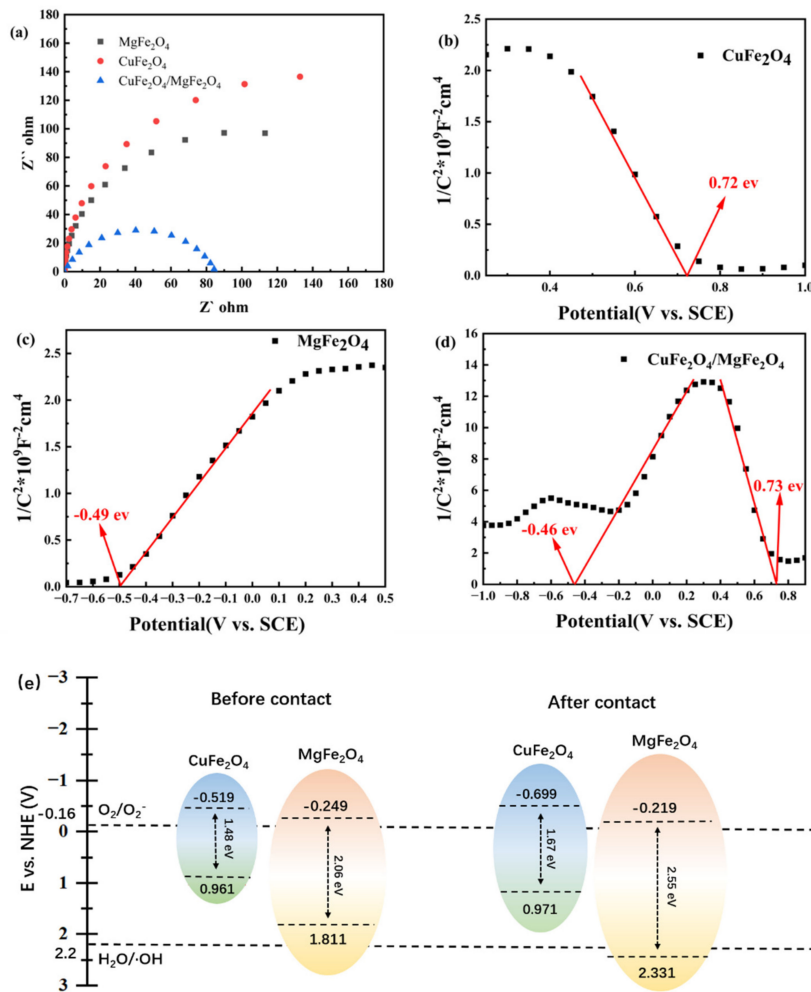


Figure 5. (a) EIS curves of the CuFe₂O₄, MgFe₂O₄ and CuFe₂O₄/MgFe₂O₄ composites; (b–d) Mott-Schottky plots of CuFe₂O₄, MgFe₂O₄ and CuFe₂O₄/MgFe₂O₄; (e) interfacial energy band diagram of the CuFe₂O₄/MgFe₂O₄ heterojunction.

The potential of the normal hydrogen electrode (NHE) of $\text{CuFe}_2\text{O}_4/\text{MgFe}_2\text{O}_4$ was calculated using Equation (9). The result was calculated as 0.961 eV for the VBM edge position of CuFe_2O_4 and -0.249 eV for the CBM edge position of MgFe_2O_4 with respect to the NHE. The Mott–Schottky plot of the $\text{CuFe}_2\text{O}_4/\text{MgFe}_2\text{O}_4$ composite (Figure 5d) shows an inverted V-shape with two regions distinguished, which is characteristic of the p-n junction formation between CuFe_2O_4 and MgFe_2O_4 [49]. Thus, the VBM of CuFe_2O_4 was located at 0.971 eV (vs. NHE) and the CBM was -0.699 eV, while the CBM of MgFe_2O_4 was located at -0.219 eV (vs. NHE) and the VBM was 2.331 eV.

2.3. Photocatalytic Experiments of the $\text{CuFe}_2\text{O}_4/\text{MgFe}_2\text{O}_4$ Composites

The degradation rates of AO_7 by the hollow composite photocatalysts with different Cu:Mg ratios (1:0.5, 1:1, 1:2, 1:3) are shown in Figure 6a, and the maximum efficiency in degrading the AO_7 over 60 min was 91.96% when the Cu:Mg ratio was 1:2, and the degradation efficiency was better than that of the other photocatalysts, shown in Table S2, over the same time. The degradation rate of 40% for the 1:2 Cu:Mg ratio under UV light was only slightly higher than that of 28% in the dark, indicating that the visible light-driven catalyzed AO_7 degradation was the dominant reaction for $\text{CuFe}_2\text{O}_4/\text{MgFe}_2\text{O}_4$. The decrease in the AO_7 concentration under dark conditions was due to the specific adsorption performance of the catalyst itself. As shown in Figure 6b,c, the light irradiation of AO_7 in aqueous solution containing (Cu:Mg = 1:2) $\text{CuFe}_2\text{O}_4/\text{MgFe}_2\text{O}_4$ suspension caused the absorbance, at 485 nm, to decrease with time and, finally, nearly disappear, indicating the destruction of its chromophore structure, with an azo and hydrazone form. The absorbance at 228 and 310 nm, attributed to the benzoic and naphthalene rings, respectively [50–52], decreased simultaneously, and no new absorption bands appeared. These results indicated the complete photocatalytic degradation of AO_7 during the reaction [53]. The linear relationship curves of the $\text{CuFe}_2\text{O}_4/\text{MgFe}_2\text{O}_4$ photocatalysts in the degradation of the AO_7 concentration with the time and quasi primary reaction kinetics are shown in Figure 6d, where C_0 and C_t are the initial concentration of AO_7 and the concentration of AO_7 during the reaction, respectively. The degradation rate of the $\text{CuFe}_2\text{O}_4/\text{MgFe}_2\text{O}_4$ photocatalyst in the AO_7 solution reached 94%. The calculated rate constant k for the $\text{CuFe}_2\text{O}_4/\text{MgFe}_2\text{O}_4$ photocatalyst was 0.0371 min^{-1} .

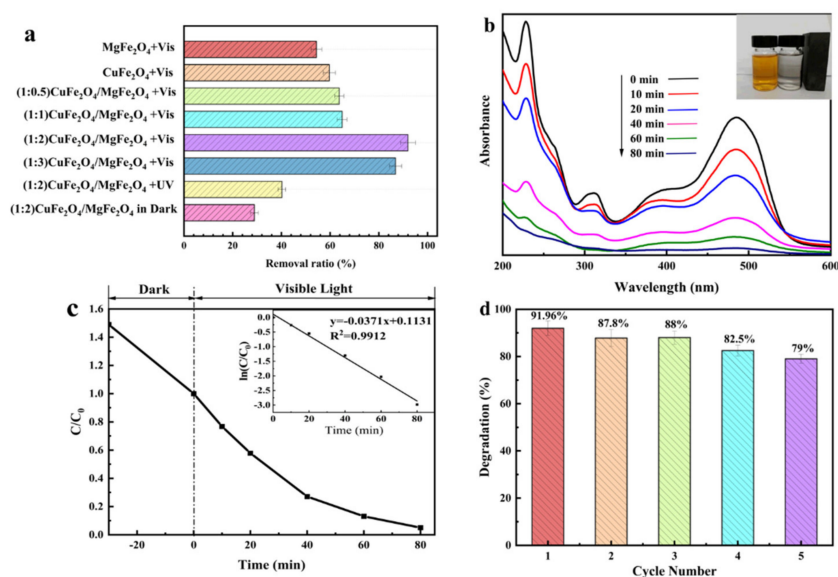


Figure 6. (a) Effects of different Cu:Mg ratios on the degradation of AO_7 ; (b) time-dependent UV–vis spectra of the AO_7 solution for (Cu:Mg = 1:2) $\text{CuFe}_2\text{O}_4/\text{MgFe}_2\text{O}_4$; (c) dark adsorption and photocatalytic degradation curves of the AO_7 solution and pseudo-first-order reaction kinetic linear relationship curve (insert; catalyst 0.8 g/L, $\text{AO}_7 = 0.10$ mM); (d) reusability of (Cu:Mg = 1:2) $\text{CuFe}_2\text{O}_4/\text{MgFe}_2\text{O}_4$ for 5 successive cycles.

The stability and reusability of catalysts are important for their practical applications. The (Cu:Mg = 1:2) $\text{CuFe}_2\text{O}_4/\text{MgFe}_2\text{O}_4$ was reused to catalyze the degradation of AO_7 over five cycles. The catalyst was magnetically separated after the reaction and washed with alcohol and dried at 60°C for every cycle. An alcohol–water system proved to be effective in the desorption of AO_7 in our prior work [54]. Figure 6d shows that the degradation rates for five cycles were 91.96%, 87%, 88%, 82% and 79%, respectively. The conversion rate decreased after the recycling due to the loss of the sample during the recycling process. The value was 79% after five cycles, demonstrating the good recyclability of the designed photocatalyst.

2.4. Mechanism of the Photocatalytic Reaction

The photocatalytic mechanism of the degradation of AO_7 by the $\text{CuFe}_2\text{O}_4/\text{MgFe}_2\text{O}_4$ was explained in detail using active species trapping experiments (Figure 7). After the addition of O_2^- [55] scavenger p-benzoquinone, h^+ scavenger ammonium oxalate [56,57] and OH^\cdot [29,56,57] propanol, the degradation rates of AO_7 were 20.8%, 49.2% and 16.3% respectively, implying that the photocatalytic mechanism was mainly controlled by the $\cdot\text{O}_2^-$ radicals and holes (h^+). In aqueous media, the redox potential of the dissolved oxygen/superoxide couple ($\text{O}_2(\text{aq.})/\text{O}_2^-$) was -0.16 eV (vs. NHE) and for the $\text{H}_2\text{O}/\cdot\text{OH}$ couple was 2.2 eV [58]. Thus, the photogenerated electrons, which are required to form superoxide, must have a potential less than -0.16 eV and photogenerated holes, needed to form $\cdot\text{OH}$, must have had a potential greater than 2.2 eV . In the case of the $\text{CuFe}_2\text{O}_4/\text{MgFe}_2\text{O}_4$ composite, the CuFe_2O_4 had the more negative balance band edge (ECB = -0.699 eV (vs. NHE) [59]) than $\text{O}_2(\text{aq.})/\cdot\text{O}_2^-$; thus, the reaction of e^- in the conduction band with the oxygen in the aqueous solution to form $\cdot\text{O}_2^-$ was thermodynamically favorable. In order to verify the role of O_2 in the photocatalytic experiments, pure N_2 was continuously bubbled into the reaction solution with a flow rate of 30 mL min^{-1} in light or dark conditions. This was followed by blowing nitrogen for 30 min in the dark to remove the O_2 from the reaction unit. The degradation rate of AO_7 was reduced to 56.11% in the presence of N_2 , which proves that O_2 is one of the main conditions required for this reaction to occur. The photogenerated h^+ in the VB of MgFe_2O_4 activated H_2O to generate $\cdot\text{OH}$, and e^- in the CB of MgFe_2O_4 reduced O_2 to $\cdot\text{O}_2^-$ radicals. Holes were retained on the VB and directly oxidative the pollutants as active species. The $\cdot\text{OH}$ had a minor contribution to the oxidative degradation of AO_7 in the $\text{CuFe}_2\text{O}_4/\text{MgFe}_2\text{O}_4$ visible light system.

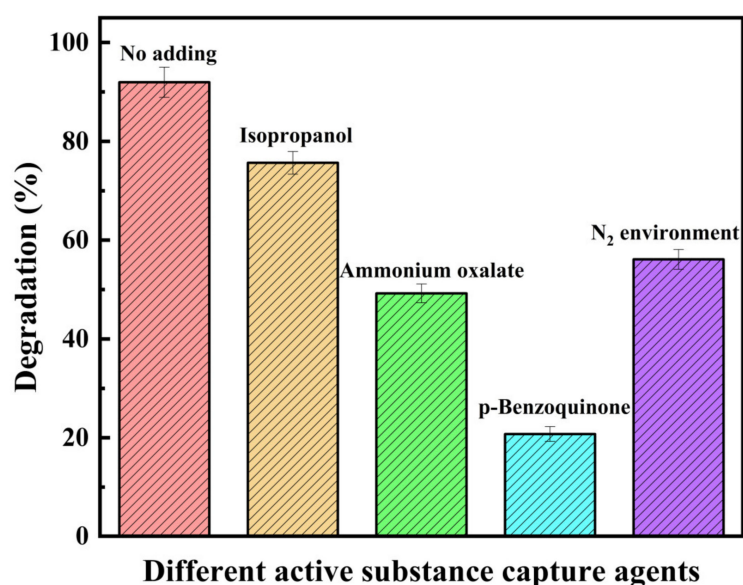


Figure 7. Effects of different scavengers on the AO_7 degradation for (Cu:Mg = 1:2) $\text{CuFe}_2\text{O}_4/\text{MgFe}_2\text{O}_4$ (catalyst 0.8 g/L, $\text{AO}_7 = 0.10\text{ mM}$, scavenger 0.1 mM).

The CB of CuFe_2O_4 was -0.699 eV (vs. NHE), and the calculated VB was 0.971 eV, based on Figure 5b–d. In a similar manner, the VB and CB of MgFe_2O_4 were measured as 2.331 eV and -0.219 eV, respectively. After absorbing the photons, the electrons of $\text{CuFe}_2\text{O}_4/\text{MgFe}_2\text{O}_4$ in the composite were able to be excited to the conduction band and leave holes in the valance band. The photogenerated e^- in the CB of CuFe_2O_4 was easily transferred to the CB of MgFe_2O_4 with the assistance of the internal electric field. This made the charge separation more effective and, hence, the electrons and holes migrated toward the surface of the respective particles and participated in the redox reaction. Simultaneously, plenty of holes gathered on the VB of CuFe_2O_4 participated in the photocatalytic reaction.

On the other hand, the dye molecules adsorbed on the photocatalyst surface could be excited by visible light photons, and the excited AO_7 had the oxidation potential of $-1.24 V_{\text{NHE}}$ ($\text{AO}_7^*/\text{AO}_7^+$) [60], which was more negative than the potential of the conduction band of the catalyst. Thus, from a thermodynamic point of view, electrons can be injected from the excited AO_7 to the conduction bands of catalyst. Here, the catalyst plays the crucial role as the electron carrier for the separation of the injected electrons and dye cation radicals. As a result, a high concentration of free electrons was formed in the conduction band of MgFe_2O_4 . These electrons reduced the dissolved oxygen into superoxide radicals ($\cdot\text{O}_2^-$), and the generated $\cdot\text{O}_2^-$ could form H_2O_2 and $\cdot\text{OH}$ under acidic conditions ($\text{pH} = 5.4$) [61]. The oxidative species could react with the AO_7 molecules and result in the degradation of the dyes. The mechanism of the degradation of AO_7 by $\text{CuFe}_2\text{O}_4/\text{MgFe}_2\text{O}_4$ under visible light is shown in Equations (1)–(5) and Figure 8.

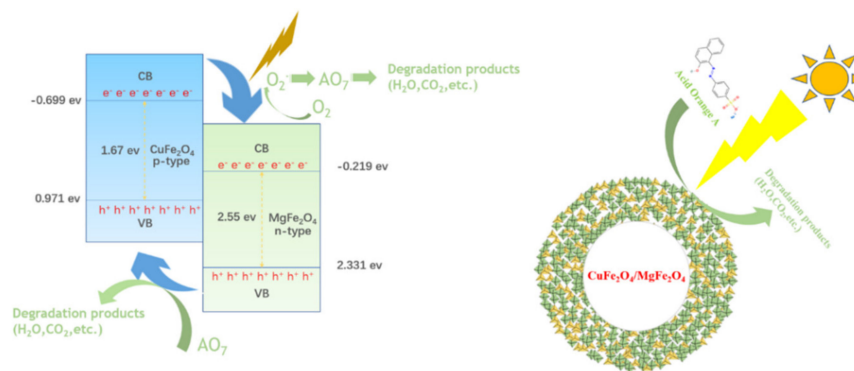
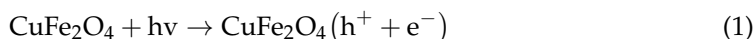


Figure 8. Schematic presentation of the electron–hole transfer by the $\text{CuFe}_2\text{O}_4/\text{MgFe}_2\text{O}_4$ photocatalyst.

3. Materials and Methods

3.1. Synthesis of $\text{CuFe}_2\text{O}_4/\text{MgFe}_2\text{O}_4$

The $\text{CuFe}_2\text{O}_4/\text{MgFe}_2\text{O}_4$ composites were fabricated via a solvothermal method with the surfactant of PEG-20000. Taking the synthesis of $\text{CuFe}_2\text{O}_4/\text{MgFe}_2\text{O}_4$ with the molar ratio of $\text{Cu}:\text{Mg} = 1:1$ in the precursors as an example, stoichiometric amounts of $\text{FeCl}_3 \cdot 6\text{H}_2\text{O}$ (5.0 mM), $\text{CuCl}_2 \cdot 2\text{H}_2\text{O}$ (1.25 mM) and $\text{MgCl}_2 \cdot 6\text{H}_2\text{O}$ (1.25 mM) were dissolved in 40 mL ethylene glycol under vigorous stirring. Under this condition, 1 g PEG-20000 and 3.6 g sodium acetate were added and kept stirring for 30 min. Then the dark-green solution was transferred into autoclaves and continued at 200°C for 8 h. The products were harvested by centrifugation, washed with distilled water and ethanol to remove unexpected ions, and dried at 60°C in air. The thus-prepared composite was denoted as

(Cu:Mg = 1:1) CuFe₂O₄/MgFe₂O₄. The different samples were prepared with varying Cu:Mg ratios = 1:0.5, 1:1, 1:2 and 1:3, respectively, while keeping the total moles of cupric chloride and magnesium chloride at 2.5 mM.

3.2. Catalyst Characterizations

X-ray diffraction (XRD) patterns were recorded with a powder diffraction system using Cu K α radiation ($\lambda = 1.5406 \text{ \AA}$) in the 2θ range of 10° – 90° . Transmission electron microscopy (TEM) images were collected on a FEI Techai 20 microscope (Hillsboro, OR, USA). High-resolution transmission electron microscopy (HRTEM) images were collected on a JEM-2100 microscope (JEOL, Tokyo, Japan) operating at an acceleration voltage of 200 kV. The diffusion reflectance spectra (DRS) were measured on an ultraviolet–visible spectrophotometer (JASCO, Tokyo, Japan, V-530). Transient photocurrents and Mott–Schottky plots were measured on an electrochemical workstation (CHI 760E, three-electrode system in 0.5 mol/L Na₂SO₄ aqueous solution as an electrolyte). The working electrode was fabricated using a drop-casting method. A total of 5 mg of the photocatalysts was dispersed in 1 mL ethanol containing 40 μ L nafion solution (5%) by sonication for 30 min. Then, the dispersive suspension was drop-cast onto a pretreated fluorine-doped tin oxide (FTO) glass substrate, and dried at 60 °C in air for 2 h to improve the adhesion. The optical properties were studied via diffuse reflectance spectroscopy in the wavelength range from 220 nm to 800 nm (DRS, Shimadzu UV-2600, Shimadzu, Kyoto, Japan).

3.3. Photocatalytic Experiments

The photocatalytic performances of the prepared ferrite composites were evaluated by the degradation of AO₇ in aqueous solution at 25 °C under simulated visible-light irradiation. A 150 W Xe lamp with 96,000 Lux was used as the light source. In a typical experiment, 0.8 g/L of the ferrite composite was dispersed in 0.10 mM AO₇ aqueous solution. Prior to irradiation, the suspension was magnetically stirred in the dark for 60 min to ensure the adsorption–desorption equilibrium. Afterwards, the solution was exposed to visible light with continuous aeration. At given time intervals, the solution was sampled and the residual concentration of AO₇ was determined by a UV-vis spectroscopy (JASCO, V-530) at 485 nm, and the degradation rate of AO₇ was determined by the following formula:

$$Q_t = \frac{(C_0 - C_t)}{C_0} \times 100\% \quad (6)$$

where Q_t is the degradation rate at time t , and C_0 and C_t are the initial concentration and concentration at time t , respectively.

The photocatalytic degradation reaction of AO₇ can be described by the pseudo-first-order kinetic, as shown in Equation (7) [62]:

$$\ln\left(\frac{C_t}{C_0}\right) = -kt \quad (7)$$

where the k is the apparent reaction rate constant.

The band gap can be estimated according to the energy dependence relation of [32]:

$$ah\nu = (h\nu - E_g)^{1/2} \quad (8)$$

where a and E_g are the absorption coefficient and the energy gap of the semiconductor, respectively. Both the CuFe₂O₄ [32,36] and MgFe₂O₄ [63] have direct band absorption.

The potential of the normal hydrogen electrode (NHE) can be converted from the obtained data by using the energy Ernst Equation (9) [64]:

$$E_{\text{NHE}} = E_{\text{SCE}} + 0.241 \quad (9)$$

where E_{NHE} corresponds to the potential of the normal hydrogen electrode after conversion, and E_{SCE} electrode indicates the collected value of the working electrode.

4. Conclusions

In summary, the magnetically recyclable $\text{CuFe}_2\text{O}_4/\text{MgFe}_2\text{O}_4$ heterojunction hollow sphere photocatalysts were prepared using a solvothermal method. The photocatalytic activity of (Cu:Mg = 1:2) $\text{CuFe}_2\text{O}_4/\text{MgFe}_2\text{O}_4$ was better than that of CuFe_2O_4 and MgFe_2O_4 , which was due to the formation of the p-n heterojunction between CuFe_2O_4 and MgFe_2O_4 . The synthesis of $\text{CuFe}_2\text{O}_4/\text{MgFe}_2\text{O}_4$ was demonstrated by XRD and XPS. The absorption edge of $\text{CuFe}_2\text{O}_4/\text{MgFe}_2\text{O}_4$ showed an obvious red shift increase following UV-Vis DRS, showing that p-n $\text{CuFe}_2\text{O}_4/\text{MgFe}_2\text{O}_4$ had a higher visible light absorption ability. The impedance of the $\text{CuFe}_2\text{O}_4/\text{MgFe}_2\text{O}_4$ heterojunction structure was lower than that of MgFe_2O_4 and CuFe_2O_4 , showing that the p-n structure promotes the separation of photogenerated carriers, and the $\text{CuFe}_2\text{O}_4/\text{MgFe}_2\text{O}_4$ material had a better photocatalytic performance. The corresponding hollow formation mechanism is proposed: $\cdot\text{O}_2^-$ and h^+ are the two main active radicals involved in the photodegradation of organic matter in the visible light $\text{CuFe}_2\text{O}_4/\text{MgFe}_2\text{O}_4$ system. Here, an efficient method for constructing hollow heterojunction-structured nanomaterials is provided for efficient photocatalytic degradation.

Supplementary Materials: The following supporting information can be downloaded at: <https://www.mdpi.com/article/10.3390/catal12080910/s1>, Figure S1: (a). The cell structure diagram of CuFe_2O_4 , (b). MgFe_2O_4 ; Figure S2: (Cu:Mg = 1:2) $\text{CuFe}_2\text{O}_4/\text{MgFe}_2\text{O}_4$ on the degradation of AO_7 ; Table S1: Element mole content table of $\text{CuFe}_2\text{O}_4/\text{MgFe}_2\text{O}_4$ by XPS; Table S2: Comparison of different reported photocatalysts for AO_7 degradation. References [65–70] are cited in the Supplementary Materials.

Author Contributions: H.X.: conceptualization, methodology, supervision and writing—original draft; Z.Z.: investigation, data curation and writing—original draft; W.C.: soft, investigation and data curation; S.R.: investigation and data curation; H.Q.: conceptualization and funding acquisition. All authors have read and agreed to the published version of the manuscript.

Funding: This work was supported by the National Natural Science Foundation of China (grant number: 51778296).

Data Availability Statement: Not applicable.

Acknowledgments: This research was funded by the National Natural Science Foundation of China grant number: 51778296.

Conflicts of Interest: The authors declare no conflict of interest or any personal circumstances or interests that may be perceived as inappropriately influencing the representation or interpretation of the reported research results. The funders had no role in the design of the study or in the collection, analysis or interpretation of the data.

References

1. Lee, M.-Y.; Wang, W.-L.; Du, Y.; Wu, Q.-Y.; Huang, N.; Xu, Z.-B.; Hu, H.-Y. Comparison of UV/ H_2O_2 and UV/PS processes for the treatment of reverse osmosis concentrate from municipal wastewater reclamation. *Chem. Eng. J.* **2020**, *388*, 79–88. [CrossRef]
2. Fu, J.; Xu, Q.; Low, J.; Jiang, C.; Yu, J. Ultrathin 2D/2D $\text{WO}_3/\text{g-C}_3\text{N}_4$ step-scheme H_2 -production photocatalyst. *Appl. Catal. B-Environ.* **2019**, *243*, 556–565. [CrossRef]
3. Masuda, Y. Bio-inspired mineralization of nanostructured TiO_2 on PET and FTO films with high surface area and high photocatalytic activity. *Sci. Rep.* **2020**, *10*, 13499–13504. [CrossRef] [PubMed]
4. Takanabe, K. Photocatalytic Water Splitting: Quantitative approaches toward photocatalyst by design. *ACS Catal.* **2017**, *7*, 8006–8022. [CrossRef]
5. Alshorifi, F.T.; Alswat, A.A.; Salama, R.S. Gold-selenide quantum dots supported onto cesium ferrite nanocomposites for the efficient degradation of rhodamine B. *Heliyon* **2022**, *8*, e09652. [CrossRef]
6. Ma, Y.; Ma, M.; Yin, X.; Shao, Q.; Lu, N.; Feng, Y.; Lu, Y.; Wujcik, E.K.; Mai, X.; Wang, C.; et al. Tuning polyaniline nanostructures via end group substitutions and their morphology dependent electrochemical performances. *Polymer* **2018**, *156*, 128–135. [CrossRef]

7. Zhang, G.; Zhang, X.; Meng, Y.; Pan, G.; Ni, Z.; Xia, S. Layered double hydroxides-based photocatalysts and visible-light driven photodegradation of organic pollutants: A review. *Chem. Eng. J.* **2020**, *392*, 123684–123690. [[CrossRef](#)]
8. Tobbala, D.E.; Rashed, A.S.; Salama, R.S.; Ahmed, T.I. Performance enhancement of reinforced concrete exposed to electrochemical magnesium chloride using nano-ferrite zinc-rich epoxy. *J. Build. Eng.* **2022**, *57*, 104869–104873. [[CrossRef](#)]
9. Umar, M.; Mahmood, N.; Awan, S.U.; Fatima, S.; Mahmood, A.; Rizwan, S. Rationally designed La and Se co-doped bismuth ferrites with controlled bandgap for visible light photocatalysis. *RSC Adv.* **2019**, *9*, 17148–17156. [[CrossRef](#)]
10. An, J.; Zhu, L.; Wang, N.; Song, Z.; Yang, Z.; Du, D.; Tang, H. Photo-Fenton like degradation of tetrabromobisphenol A with graphene/BiFeO₃ composite as a catalyst. *Chem. Eng. J.* **2013**, *219*, 225–237. [[CrossRef](#)]
11. Li, Z.; Shen, Y.; Yang, C.; Lei, Y.; Guan, Y.; Lin, Y.; Liu, D.; Nan, C.-W. Significant enhancement in the visible light photocatalytic properties of BiFeO₃–graphene nanohybrids. *J. Mater. Chem. A* **2013**, *1*, 823–829. [[CrossRef](#)]
12. Kazachenko, A.S.; Vasilieva, N.Y.; Fetisova, O.Y.; Sychev, V.V.; Elsuif'ev, E.V.; Malyar, Y.N.; Issaoui, N.; Miroshnikova, A.V.; Borovkova, V.S.; Kazachenko, A.S.; et al. New reactions of betulin with sulfamic acid and ammonium sulfamate in the presence of solid catalysts. *Biomass Convers. Biorefinery* **2022**, *23*, 02587–02591. [[CrossRef](#)]
13. Zhu, Y.; Liu, Y.; Ai, Q.; Gao, G.; Yuan, L.; Fang, Q.; Tian, X.; Zhang, X.; Egap, E.; Ajayan, P.M.; et al. In situ synthesis of lead-free halide perovskite-COF nanocomposites as photocatalysts for photoinduced polymerization in both organic and aqueous phases. *ACS Mater. Lett.* **2022**, *4*, 464–471. [[CrossRef](#)]
14. Bajpai, O.P.; Mandal, S.; Ananthakrishnan, R.; Mandal, P.; Khastgir, D.; Chattopadhyay, S. Structural features, magnetic properties and photocatalytic activity of bismuth ferrite nanoparticles grafted on graphene nanosheets. *New J. Chem.* **2018**, *42*, 10712–10723. [[CrossRef](#)]
15. Yin, X.L.; Liu, J.; Jiang, W.J.; Zhang, X.; Hu, J.S.; Wan, L.J. Urchin-like Au@CdS/WO₃ micro/nano heterostructure as a visible-light driven photocatalyst for efficient hydrogen generation. *Chem. Commun.* **2015**, *51*, 13842–13845. [[CrossRef](#)]
16. Chakraborty, I.; Rakshit, R.; Mandal, K. Synthesis and functionalization of MnFe₂O₄ nano-hollow spheres for novel optical and catalytic properties. *Surf. Interfaces* **2017**, *7*, 106–112. [[CrossRef](#)]
17. Cheng, C.; Zhang, H.; Ren, W.; Dong, W.; Sun, Y. Three dimensional urchin-like ordered hollow TiO₂/ZnO nanorods structure as efficient photoelectrochemical anode. *Nano Energy* **2013**, *2*, 779–786. [[CrossRef](#)]
18. Cui, X.; Jiang, G.; Zhu, M.; Zhao, Z.; Du, L.; Weng, Y.; Xu, C.; Zhang, D.; Zhang, Q.; Wei, Y.; et al. TiO₂/CdS composite hollow spheres with controlled synthesis of platinum on the internal wall for the efficient hydrogen evolution. *Int. J. Hydrogen Energy* **2013**, *38*, 9065–9073. [[CrossRef](#)]
19. Amuthan, T.; Sanjeevi, R.; Kannan, G.R.; Sridevi, A. A novel p-CuFe₂O₄/n-ZnS heterojunction photocatalyst: Co-precipitation synthesis, characterization and improved visible-light driven photocatalytic activity for removal of MB and CV dyes. *Phys. B Condens. Matter* **2022**, *638*, 413842–413848. [[CrossRef](#)]
20. Mousavi, M.; Habibi, M.M.; Zhang, G.; Pourhakkak, P.; Moradian, S.; Ghasemi, J.B. In-situ construction of ZnO/Sb₂MoO₆ nano-heterostructure for efficient visible-light photocatalytic conversion of N₂ to NH₃. *Surf. Interfaces* **2022**, *30*, 101844. [[CrossRef](#)]
21. Wang, Z.; Lin, Z.; Shen, S.; Zhong, W.; Cao, S. Advances in designing heterojunction photocatalytic materials. *Chin. J. Catal.* **2021**, *42*, 710–730. [[CrossRef](#)]
22. Jang, J.S.; Kim, H.G.; Lee, J.S. Heterojunction semiconductors: A strategy to develop efficient photocatalytic materials for visible light water splitting. *Catal. Today* **2012**, *185*, 270–277. [[CrossRef](#)]
23. Yan, Y.; Zeng, Z.; Huang, M.; Chen, P. Van der waals heterojunctions for catalysis. *Mater. Today Adv.* **2020**, *6*, 100059–100063. [[CrossRef](#)]
24. Arimi, A.; Megatif, L.; Granone, L.I.; Dillert, R.; Bahnemann, D.W. Visible-light photocatalytic activity of zinc ferrites. *J. Photochem. Photobiol. A-Chem.* **2018**, *366*, 118–126. [[CrossRef](#)]
25. Lenin, N.; Kanna, R.R.; Sakthipandi, K.; Kumar, A.S. Structural, electrical and magnetic properties of NiLa_xFe_{2-x}O₄ nanoferrites. *Mater. Chem. Phys.* **2018**, *212*, 385–393. [[CrossRef](#)]
26. Alshorifi, F.T.; Ali, S.L.; Salama, R.S. Promotional synergistic effect of Cs–Au NPs on the performance of Cs–Au/MgFe₂O₄ catalysts in catalysis 3,4-Dihydropyrimidin-2(1H)-Ones and degradation of RhB Dye. *J. Inorg. Organomet. Polym. Mater.* **2022**, *8*, 02389–02401. [[CrossRef](#)]
27. Kumar, G.M.; Cho, H.D.; Lee, D.J.; Kumar, J.R.; Siva, C.; Ilanchezhian, P.; Kim, D.Y.; Kang, T.W. Elevating the charge separation of MgFe₂O₄ nanostructures by Zn ions for enhanced photocatalytic and photoelectrochemical water splitting. *Chemosphere* **2021**, *283*, 131134–131145. [[CrossRef](#)]
28. Kim, H.G.; Borse, P.H.; Jang, J.S.; Jeong, E.D.; Jung, O.-S.; Suh, Y.J.; Lee, J.S. Fabrication of CaFe₂O₄/MgFe₂O₄ bulk heterojunction for enhanced visible light photocatalysis. *Chem. Commun.* **2009**, *279*, 5889–5891. [[CrossRef](#)]
29. Fan, W.; Li, M.; Bai, H.; Xu, D.; Chen, C.; Li, C.; Ge, Y.; Shi, W. Fabrication of MgFe₂O₄/MoS₂ heterostructure nanowires for photoelectrochemical catalysis. *Langmuir* **2016**, *32*, 1629–1636. [[CrossRef](#)]
30. Liu, X.; An, S.; Shi, W.; Yang, Q.; Zhang, L. Microwave-induced catalytic oxidation of malachite green under magnetic Cu-ferrites: New insight into the degradation mechanism and pathway. *J. Mol. Catal. A Chem.* **2014**, *395*, 243–250. [[CrossRef](#)]
31. Wang, Y.; Zhao, H.; Li, M.; Fan, J.; Zhao, G. Magnetic ordered mesoporous copper ferrite as a heterogeneous Fenton catalyst for the degradation of imidacloprid. *Appl. Catal. B-Environ.* **2014**, *147*, 534–545. [[CrossRef](#)]
32. Shen, Y.; Wu, Y.; Xu, H.; Fu, J.; Li, X.; Zhao, Q.; Hou, Y. Facile preparation of sphere-like copper ferrite nanostructures and their enhanced visible-light-induced photocatalytic conversion of benzene. *Mater. Res. Bull.* **2013**, *48*, 4216–4222. [[CrossRef](#)]

33. Sharma, R.; Kumar, V.; Bansal, S.; Singhal, S. Assortment of magnetic nanospinels for activation of distinct inorganic oxidants in photo-Fenton's process. *J. Mol. Catal. A-Chem.* **2015**, *402*, 53–63. [[CrossRef](#)]
34. Ilhan, S.; Izotova, S.G.; Komlev, A.A. Synthesis and characterization of MgFe₂O₄ nanoparticles prepared by hydrothermal decomposition of co-precipitated magnesium and iron hydroxides. *Ceram. Int.* **2015**, *41*, 577–585. [[CrossRef](#)]
35. Derbal, A.; Omeiri, S.; Bouguelia, A.; Trari, M. Characterization of new heterosystem CuFeO₂/SnO₂ application to visible-light induced hydrogen evolution. *Int. J. Hydrogen Energy* **2008**, *33*, 4274–4282. [[CrossRef](#)]
36. Fedailaine, M.; Bellal, B.; Berkani, S.; Trari, M.; Abdi, A. Photo-electrochemical characterization of the spinel CuFe₂O₄: Application to Ni²⁺ removal under solar light. *Environ. Process.* **2016**, *3*, 387–396. [[CrossRef](#)]
37. Dom, R.; Subasri, R.; Radha, K.; Borse, P.H. Synthesis of solar active nanocrystalline ferrite, MFe₂O₄ (M: Ca, Zn, Mg) photocatalyst by microwave irradiation. *Solid State Commun.* **2011**, *151*, 470–473. [[CrossRef](#)]
38. Feizpoor, S.; Habibi-Yangjeh, A.; Vadivel, S. Novel TiO₂/Ag₂CrO₄ nanocomposites: Efficient visible-light-driven photocatalysts with n-n heterojunctions. *J. Photochem. Photobiol. A-Chem.* **2017**, *341*, 57–68. [[CrossRef](#)]
39. Gu, X.; Li, C.; Yuan, S.; Ma, M.; Qiang, Y.; Zhu, J. ZnO based heterojunctions and their application in environmental photocatalysis. *Nanotechnology* **2016**, *27*, 402001–402013. [[CrossRef](#)]
40. Yan, Y.; Guan, H.; Liu, S.; Jiang, R. Ag₃PO₄/Fe₂O₃ composite photocatalysts with an n-n heterojunction semiconductor structure under visible-light irradiation. *Ceram. Int.* **2014**, *40*, 9095–9100. [[CrossRef](#)]
41. Zou, X.; Dong, Y.; Zhang, X.; Cui, Y.; Ou, X.; Qi, X. The highly enhanced visible light photocatalytic degradation of gaseous odichlorobenzene through fabricating like-flowers BiPO₄/BiOBr p-n heterojunction composites. *Appl. Surf. Sci.* **2017**, *391*, 525–534. [[CrossRef](#)]
42. Wang, X.; Feng, J.; Bai, Y.; Zhang, Q.; Yin, Y. Synthesis, Properties, and Applications of Hollow Micro-/Nanostructures. *Chem. Rev.* **2016**, *116*, 10983–11060. [[CrossRef](#)]
43. Gabal, M.A.; Al-luhaibi, R.S.; Al Angari, Y.M. Mn-Zn nano-crystalline ferrites synthesized from spent Zn-C batteries using novel gelatin method. *J. Hazard. Mater.* **2013**, *246*, 227–233. [[CrossRef](#)]
44. Sharma, R.; Bansal, S.; Singhal, S. Tailoring the photo-Fenton activity of spinel ferrites (MFe₂O₄) by incorporating different cations (M = Cu, Zn, Ni and Co) in the structure. *RSC Adv.* **2015**, *5*, 6006–6018. [[CrossRef](#)]
45. Yin, Y.; Liu, W.; Huo, N.; Yang, S. High rate capability and long cycle stability of Fe₂O₃/MgFe₂O₄ anode material synthesized by gelcast processing. *Chem. Eng. J.* **2017**, *307*, 999–1007. [[CrossRef](#)]
46. Zhang, L.; Ghimire, P.; Phuriragpitikhon, J.; Jiang, B.; Goncalves, A.A.S.; Jaroniec, M. Facile formation of metallic bismuth/bismuth oxide heterojunction on porous carbon with enhanced photocatalytic activity. *J. Colloid Interface Sci.* **2018**, *513*, 82–91. [[CrossRef](#)]
47. Wen, X.-J.; Niu, C.-G.; Zhang, L.; Liang, C.; Zeng, G.-M. An in depth mechanism insight of the degradation of multiple refractory pollutants via a novel SrTiO₃/BiOI heterojunction photocatalysts. *J. Catal.* **2017**, *356*, 283–299. [[CrossRef](#)]
48. Huu, H.T.; Thi, M.D.N.; Nguyen, V.P.; Thi, L.N.; Phan, T.T.T.; Hoang, Q.D.; Luc, H.H.; Kim, S.J.; Vo, V. One-pot synthesis of S-scheme MoS₂/g-C₃N₄ heterojunction as effective visible light photocatalyst. *Sci. Rep.* **2021**, *11*, 14787. [[CrossRef](#)]
49. Wen, X.-J.; Niu, C.-G.; Zhang, L.; Liang, C.; Zeng, G.-M. A novel Ag₂O/CeO₂ heterojunction photocatalysts for photocatalytic degradation of enrofloxacin: Possible degradation pathways, mineralization activity and an in depth mechanism insight. *Appl. Catal. B-Environ.* **2018**, *221*, 701–714. [[CrossRef](#)]
50. Barros, V.P.; Assis, M.D. Iron porphyrins as biomimetical models for disperse azo dye oxidation. *J. Braz. Chem. Soc.* **2013**, *24*, 830–836. [[CrossRef](#)]
51. Wu, F.; Deng, N.S.; Hua, H.L. Degradation mechanism of azo dye C.I. reactive red 2 by iron powder reduction and photooxidation in aqueous solutions. *Chemosphere* **2000**, *41*, 1233–1238. [[CrossRef](#)]
52. Zhang, S.J.; Yu, H.Q.; Li, Q.R. Radiolytic degradation of Acid Orange 7: A mechanistic study. *Chemosphere* **2005**, *61*, 1003–1011. [[CrossRef](#)]
53. Li, X.; Hou, Y.; Zhao, Q.; Wang, L. A general, one-step and template-free synthesis of sphere-like zinc ferrite nanostructures with enhanced photocatalytic activity for dye degradation. *J. Colloid Interface Sci.* **2011**, *358*, 102–108. [[CrossRef](#)]
54. Xing, X.; Qu, H.; Shao, R.; Wang, Q.; Xie, H. Mechanism and kinetics of dye desorption from dye-loaded carbon (XC-72) with alcohol-water system as desorbent. *Water Sci. Technol.* **2017**, *76*, 1243–1250. [[CrossRef](#)]
55. Styliidi, M.; Kondarides, D.I.; Verykios, X.E. Visible light-induced photocatalytic degradation of Acid Orange 7 in aqueous TiO₂ suspensions. *Appl. Catal. B-Environ.* **2004**, *47*, 189–201. [[CrossRef](#)]
56. Liang, S.; Zhu, S.; Chen, Y.; Wu, W.; Wang, X.; Wu, L. Rapid template-free synthesis and photocatalytic performance of visible light-activated SnNb₂O₆ nanosheets. *J. Mater. Chem.* **2012**, *22*, 2670–2678. [[CrossRef](#)]
57. Su, M.; He, C.; Sharma, V.K.; Abou Asi, M.; Xia, D.; Li, X.-Z.; Deng, H.; Xiong, Y. Mesoporous zinc ferrite: Synthesis, characterization, and photocatalytic activity with H₂O₂/visible light. *J. Hazard. Mater.* **2012**, *211*, 95–103. [[CrossRef](#)]
58. Li, Y.; Zhang, W.; Niu, J.; Chen, Y. Mechanism of photogenerated reactive oxygen species and correlation with the antibacterial properties of engineered metal-oxide nanoparticles. *ACS Nano* **2012**, *6*, 5164–5173. [[CrossRef](#)]
59. Hussain, S.; Hussain, S.; Waleed, A.; Tavakoli, M.M.; Wang, Z.; Yang, S.; Fan, Z.; Nadeem, M.A. Fabrication of CuFe₂O₄/alpha-Fe₂O₃ composite thin films on FTO coated glass and 3-D nanospine structures for efficient photoelectrochemical water splitting. *ACS Appl. Mater. Interfaces* **2016**, *8*, 35315–35322. [[CrossRef](#)]

60. Nasr, C.; Vinodgopal, K.; Fisher, L.; Hotchandani, S.; Chattopadhyay, A.K.; Kamat, P.V. Environmental photochemistry on semiconductor surfaces. Visible light induced degradation of a textile diazo dye, naphthol blue black, on TiO₂ nanoparticles. *J. Phys. Chem.* **1996**, *100*, 8436–8442. [[CrossRef](#)]
61. Wen, X.-J.; Niu, C.-G.; Huang, D.-W.; Zhang, L.; Liang, C.; Zeng, G.-M. Study of the photocatalytic degradation pathway of norfloxacin and mineralization activity using a novel ternary Ag/AgCl-CeO₂ photocatalyst. *J. Catal.* **2017**, *355*, 73–86. [[CrossRef](#)]
62. Bechambi, O.; Jlaiel, L.; Najjar, W.; Sayadi, S. Photocatalytic degradation of bisphenol A in the presence of Ce-ZnO: Evolution of kinetics, toxicity and photodegradation mechanism. *Mater. Chem. Phys.* **2016**, *173*, 95–105. [[CrossRef](#)]
63. Zhang, J.; Yan, M.; Sun, G.; Li, X.; Liu, K. Visible-light photo-Fenton catalytic MgFe₂O₄ spinel: Reaction sintering synthesis and DFT study. *J. Alloy. Compd.* **2021**, *889*, 161673–161684. [[CrossRef](#)]
64. Hao, X.; Hu, Z.; Xiang, D.; Jin, Z. Construction of CdS@Cu_{2-x}S core-shell p-n heterojunction with enhanced charge separation for wide spectrum photocatalytic H₂ evolution. *Mol. Catal.* **2022**, *528*, 112417–112431. [[CrossRef](#)]
65. Huang, T.; Mao, S.; Yu, J.; Wen, Z.; Lu, G.; Chen, J. Effects of N and F doping on structure and photocatalytic properties of anatase TiO₂ nanoparticles. *RSC Adv.* **2013**, *3*, 16657–16664. [[CrossRef](#)]
66. Baliarsingh, N.; Parida, K.M.; Pradhan, G.C. Effects of Co, Ni, Cu, and Zn on Photophysical and Photocatalytic Properties of Carbonate Intercalated MII/Cr LDHs for Enhanced Photodegradation of Methyl Orange. *Ind. Eng. Chem. Res.* **2014**, *53*, 3834–3841. [[CrossRef](#)]
67. Yan, S.; Wang, B.; Shi, Y.; Yang, F.; Hu, D.; Xu, X.; Wu, J. Hydrothermal synthesis of CdS nanoparticle/functionalized graphene sheet nanocomposites for visible-light photocatalytic degradation of methyl orange. *Appl. Surf. Sci.* **2013**, *285*, 840–845. [[CrossRef](#)]
68. Chen, Q.; Wu, L.; Zhao, X.; Yang, X.-J. Fabrication of Zn-Ti layered double oxide nanosheets with ZnO/ZnTiO₃ heterojunction for enhanced photocatalytic degradation of MO, RhB and MB. *J. Mol. Liq.* **2022**, *353*, 118794. [[CrossRef](#)]
69. Xu, M.L.; Jiang, X.J.; Li, J.R.; Wang, F.J.; Li, K.; Cheng, X. Self-Assembly of a 3D Hollow BiOBr@Bi-MOF Heterostructure with Enhanced Photocatalytic Degradation of Dyes. *ACS Appl. Mater. Interfaces* **2021**, *13*, 56171–56180. [[CrossRef](#)]
70. Ma, M.; Yang, Y.; Chen, Y.; Jiang, J.; Ma, Y.; Wang, Z.; Huang, W.; Wang, S.; Liu, M.; Ma, D.; et al. Fabrication of hollow flower-like magnetic Fe₃O₄/C/MnO₂/C₃N₄ composite with enhanced photocatalytic activity. *Sci. Rep.* **2021**, *11*, 2597. [[CrossRef](#)]